H0LiCOW VIII. A weak-lensing measurement of the external convergence in the field of the lensed quasar HE 0435−1223

O. Tihhonova,[1]⋆ F. Courbin,[1] D. Harvey,[1] S. Hilbert,[2,3] C. E. Rusu,[4,5] C. D. Fassnacht,[4] V. Bonvin,[1] P. J. Marshall,[6] G. Meylan,[1] D. Sluse,[7] S. H. Suyu,[8,9,10] T. Treu[11] and K. C. Wong[12]

[1]*Laboratoire d'Astrophysique, Ecole Polytechnique Fédérale de Lausanne (EPFL), Observatoire de Sauverny, CH-1290 Versoix, Switzerland*
[2]*Exzellenzcluster Universe, Boltzmannstr. 2, D-85748 Garching, Germany*
[3]*Ludwig-Maximilians-Universität, Universitäts-Sternwarte, Scheinerstr. 1, D-81679 München, Germany*
[4]*Department of Physics, University of California, Davis, CA 95616, USA*
[5]*Subaru Telescope, 650 N Aohoku Pl, Hilo, HI 96720, USA*
[6]*Kavli Institute for Particle Astrophysics and Cosmology, Stanford University, 452 Lomita Mall, Stanford, CA 94035, USA*
[7]*STAR Institute, Quartier Agora - Allée du six Août, 19c B-4000 Liège, Belgium*
[8]*Max-Planck-Institut für Astrophysik, Karl-Schwarzschild-Str. 1, D-85748 Garching, Germany*
[9]*Institute of Astronomy and Astrophysics, Academia Sinica, PO Box 23-141, Taipei 10617, Taiwan*
[10]*Physik Department, Technische Universität München, James-Franck-Straße 1, D-85748 Garching, Germany*
[11]*Department of Physics and Astronomy, University of California, Los Angeles, CA 90095, USA*
[12]*National Astronomical Observatory of Japan, 2-21-1 Osawa, Mitaka, Tokyo 181-8588, Japan*

ABSTRACT

We present a weak gravitational lensing measurement of the external convergence along the line of sight to the quadruply lensed quasar HE 0435−1223. Using deep r-band images from Subaru Suprime Cam, we observe galaxies down to a 3σ limiting magnitude of ∼26 mag resulting in a source galaxy density of 14 galaxies per square arcminute after redshift-based cuts. Using an inpainting technique and multiscale entropy filtering algorithm, we find that the region in close proximity to the lens has an estimated external convergence of $\kappa = -0.012^{+0.020}_{-0.013}$ and is hence marginally underdense. We also rule out the presence of any halo with a mass greater than $M_{\rm vir} = 1.6 \times 10^{14} h^{-1} M_\odot$ (68 per cent confidence limit). Our results, consistent with previous studies of this lens, confirm that the intervening mass along the line of sight to HE 0435−1223 does not affect significantly the cosmological results inferred from the time-delay measurements of that specific object.

Key words: gravitational lensing: weak – quasars: individual: HE 0435−1223 – cosmological parameters – distance scale.

1 INTRODUCTION

In the strong regime, gravitational lensing by a galaxy-scale object can produce multiple images of the background light source. As the light rays forming the images are taking different paths to reach the observer plane, there exists a delay in the arrival time of the photons. Refsdal (1964) was the first to propose the use of these time delays as a tool for cosmography. Time delays are proportional to the gravitational potential of the deflector and its gradient, and to the combination of three angular diameter distances of the observer–lens–source system, dubbed the time-delay distance (Schneider, Kochanek & Wambsganss 2006; Suyu et al. 2010). The

latter is inversely proportional to the Hubble constant H_0 and has a weaker dependence on the other cosmological parameters, notably curvature, and dark energy (e.g. Coe & Moustakas 2009).

In practice, the values of the time delays of the lensed images are obtained by measuring the time shift between their light curves, provided they show significant variability. Although the original idea of Refsdal (1964) was to use lensed supernovae (resolved ones found only recently, e.g. Kelly et al. 2015; Rodney et al. 2015; Goobar et al. 2017), time delays have been first measured in lensed quasars (e.g. Vanderriest et al. 1989; Schild 1990; Lehar et al. 1992). This provided a new way to obtain independent estimates of the Hubble constant H_0 (e.g. Suyu et al. 2017; Bonvin et al. 2017), complementary to and competitive with other probes such as the cosmic microwave background (CMB, Planck Collaboration et al. 2016), baryon acoustic oscillations (BAO) + CMB (Alam

⋆ E-mail: olga.tihhonova@epfl.ch

et al. 2017), weak lensing + BAO + big bang nucleosynthesis (DES Collaboration et al. 2017), Cepheids (Freedman et al. 2012), type Ia supernovae (Riess et al. 2016), megamasers (Reid et al. 2013), giant ionized H_2 regions (Fernández Arenas et al. 2018), and standard sirens (Abbott et al. 2017).

The H0LiCOW program (H_0 Lenses in COSMOGRAIL's Wellspring; Suyu et al. 2017) is devoted to the measurement of H_0 using lensing time delays. When completed, the goal of the first phase of the program is to measure H_0 to below 3.5 per cent precision with five gravitationally lensed quasar systems (B1608+656, RXJ1131−1231, HE 0435−1223 WFI2033−4723, and HE1104−1805). It mostly uses optical time-delay measurements from the COSMOGRAIL collaboration (the COSmological MOnitoring of GRAvItational Lenses; e.g. Courbin et al. 2005, 2011; Bonvin et al. 2016), but also the radio time delays for the quadruply imaged quasar B1608+656 (Fassnacht et al. 2002). In addition, H0LiCOW enables detailed study of quasar host galaxies, taking the advantage of the lensing magnifications (Ding et al. 2017a,b).

In order to recover the cosmological information from an individual lens system with high precision and accuracy, the following steps are required: (i) time-delay measurements, (ii) modelling of the mass of the deflector using the lensing and stellar kinematic data, (iii) modelling of the environment and the line of sight (env&los) of the deflector (see Treu & Marshall 2016 for the detailed review). The H0LiCOW collaboration addresses all three steps (e.g. Bonvin et al. 2017; Wong et al. 2017; Sluse et al. 2017; Rusu et al. 2017). In this work, we focus specifically on the third step, which is needed alongside the second one in order to break the lensing degeneracies inherent to the mass-sheet transformation (MST, Falco, Gorenstein & Shapiro 1985; Schneider & Sluse 2013).

The MST is a modification of the mass distribution which leaves all image positions, shapes, and flux ratios invariant, but changes the product of Hubble constant and time delay $H_0 \Delta t$. It corresponds to the rescaling of the deflector mass by introducing a 'mass sheet', which can be represented by a constant over- or underdensity along the line of sight and around the lens. Two types of mass sheets can be distinguished: internal and external. The internal mass sheet is physically associated with the lens. The external mass sheet, on the contrary, is due to the intervening objects which do not lie in the immediate vicinity of the lens, and is thus not physically associated with it. As a consequence, the latter cannot be fully constrained by measurements of the kinematics of the main lens (e.g. Koopmans 2004). Modelling of the env&los becomes mandatory. The external mass sheet can be approximated by the dimensionless surface mass density or convergence κ_{ext} at the position of the main lens. The impact of κ_{ext} on the Hubble constant can be expressed as

$$H_0^{true} = (1 - \kappa_{ext}) \times H_0^{model}, \tag{1}$$

where H_0^{model} is the Hubble constant obtained from the model with no account for the env&los. Thus, neglecting the presence of an overdense env&los (compared with the rest of the Universe) will result in H_0^{model} overestimating the true value of Hubble constant H_0^{true}. An underdense line of sight will have, of course, the opposite effect. For a single system, if uncorrected for, this bias can reach up to several percent (Keeton & Zabludoff 2004; Jaroszyński & Skowron 2016; McCully et al. 2017a). The effect may not average out for the ensemble of lenses either, since due to the selection and by virtue of the lenses being typically massive ellipticals, lensed systems may be preferably observed in overdense environments (Collett & Cunnington 2016).

The effects of env&los have been evaluated in several ways. For example, Momcheva et al. (2006), Fassnacht et al. (2006),

Auger et al. (2007), and Wilson et al. (2017) estimated κ_{ext} by fitting analytical mass profiles to the spectroscopically confirmed groups found in the vicinity of the lens systems. Collett et al. (2013) combined the halo mass model approach with the calibration to the Millennium Simulation (MS, Springel et al. 2005), making use of the ray-tracing calculations of convergence by Hilbert et al. (2009a).

Suyu et al. (2010) compared galaxy number counts in the field around the lens from Fassnacht, Koopmans & Wong (2011) to the mock fields drawn from the MS. They measured κ_{ext} in simulated fields having the same statistical properties as the real data. Greene et al. (2013) extended this technique by weighting the galaxy counts by distance, photometric redshift, and stellar mass.

Birrer et al. (2017) combined the study of the environment using the halo-rendering approach, i.e. linking the galaxy stellar masses to the underlying mass distribution, with the external shear measurements of the strong lens system. Their combined approach yielded tighter constraints on the inferred external convergence compared to a halo-rendering approach only.

Finally, Fischer et al. (1997), Nakajima et al. (2009), and Fadely et al. (2010) followed a different approach relying on the weak-lensing effect produced by massive structures in the vicinity of the deflector. They constrained the external convergence by integrating the tangential weak gravitational shear in the area around the lens. McCully et al. (2017a) computed the weak-lensing contamination preserving the full 3D mass distribution by using a hybrid multiplane lensing formalism (McCully et al. 2014).

In this work, we measure the env&los of the quadruply lensed quasar HE 0435−1223 (Wisotzki et al. 2000, 2002), using the weak gravitational lensing technique. This method is direct and complementary to the env&los study by Rusu et al. (2017, hereafter H0LiCOW III), which uses the galaxy number counts technique. The goal of our analysis is twofold. First, we estimate κ_{ext} all the way to the redshift of the lensed quasar. Second, we test the hypothesis that the main lens may be embedded in a massive halo affecting the overall mass modelling.

The paper is organized as follows. Section 2 contains a brief overview of weak gravitational lensing and mass reconstruction formalism. We describe in Section 3 the Subaru Suprime-Cam images used for the analysis, how we deal with masks, and the final galaxy selection. Section 4 comprises the reconstruction and filtering of the convergence field, and the corrections for the lensing efficiency. Our estimates of the line-of-sight external convergence are given in Section 5. In Section 6, we test for the possible presence of a halo at a single redshift along the line of sight to the quasar, and outline the numerical simulations used to estimate the efficiency of our technique to detect such a halo, given the data. Finally, we draw our conclusions in Section 7.

We adopt a flat Λ cold dark matter (ΛCDM)cosmology with $\Omega_M = 0.3$, $\Omega_\Lambda = 0.7$, and $H_0 = 70 \, \mathrm{km \, s^{-1} Mpc^{-1}}$ when producing mocks of observations. Note that the details of the cosmology chosen here have no significant effect.

2 WEAK GRAVITATIONAL LENSING FORMALISM

We summarize the formalism for weak gravitational lensing studies, from the measurement of the ellipticities of galaxies to the reconstruction of mass maps. We focus on the specific application of measuring κ_{ext} along a given line of sight. A detailed general description of weak gravitational lensing can be found, in e.g. Bartelmann & Schneider (2001).

2.1 Principles of weak gravitational lensing

Weak gravitational lensing manifests itself as coherent distortions of the images of distant galaxies. The effect is due to the deflection of light rays while they are propagating through an inhomogeneous gravitational field. The measure of the distortions is sensitive to the mass distribution projected along the line of sight, and depends neither on the nature nor on the physical state of the matter, hence making weak lensing an efficient mass probe.

Weak gravitational lensing changes the apparent size, shape, and magnitude of distant galaxies. The shape distortion, described by the complex shear γ, is a stretch of the image due to the 3D tidal gravitational field of the foreground mass. In the Born approximation, for sources at a single redshift z_s the 3D matter distribution of the lens can be considered as an equivalent plane with a deflection potential ψ (Schneider et al. 2006). The complex shear field can be expressed as:

$$\gamma(\boldsymbol{\theta}, z_s) = \gamma_1 + i\gamma_2 = \frac{1}{2}\left(\frac{\partial^2\psi}{\partial\theta_1^2} - \frac{\partial^2\psi}{\partial\theta_2^2}\right) + i\frac{\partial^2\psi}{\partial\theta_1\partial\theta_2}, \quad (2)$$

where $\boldsymbol{\theta}$ is the 2D angular position on the sky, z_s is the source redshift, and ψ is the 2D deflection potential described by

$$\psi(\boldsymbol{\theta}, z_s) = \frac{2}{c^2}\int_0^{z_s}\frac{D_{ds}}{D_{os}D_{od}}\,\Phi(\boldsymbol{\theta}, z)\,dz, \quad (3)$$

where D_{od}, D_{ds}, and D_{os} are the angular diameter distances between the observer and the deflector, the deflector and the source, and the observer and the source respectively, c is the speed of light, and $\Phi(\boldsymbol{\theta}, z)$ is the 3D gravitational potential of the deflector in the redshift interval dz.

The change in image size is caused by both anisotropic focusing of light by the tidal gravitational field, and by isotropic focusing by the local matter density. The latter is usually expressed in terms of the dimensionless effective surface mass density or convergence κ:

$$\kappa(\boldsymbol{\theta}, z_s) = \int_0^{z_s}\frac{\Sigma(\boldsymbol{\theta}, z)}{\Sigma_{crit}}\,dz, \quad (4)$$

where $\Sigma(\boldsymbol{\theta}, z)$ is the surface mass density in the redshift interval dz, and Σ_{crit} is the critical surface mass density

$$\Sigma_{crit} = \frac{c^2}{4\pi G}\frac{D_{os}}{D_{od}D_{ds}}, \quad (5)$$

where G is the gravitational constant. Convergence can also be expressed in terms of the deflection potential:

$$\kappa(\boldsymbol{\theta}) = \frac{1}{2}\left(\frac{\partial^2\psi}{\partial\theta_1^2} + \frac{\partial^2\psi}{\partial\theta_2^2}\right). \quad (6)$$

In practice, lensed sources are not located at a single redshift z_s, but rather span a redshift interval with a given distribution $p(z_s)$. This allows us to define an effective surface mass density

$$\kappa(\boldsymbol{\theta}) = \int_0^{z_{max}}\kappa(\boldsymbol{\theta}, z_s)\,p(z_s)\,dz_s. \quad (7)$$

where the mass is integrated along the line of sight up to a maximum redshift z_{max}.

The presence of matter at different redshifts deviates from the assumption used for the Born approximation. This deviation for the derived convergence value is, however, of order of 1 per cent (e.g. Petri, Haiman & May 2017). As this is smaller than the statistical errors due to the galaxy number density in our analysis, we would not consider here any additional corrections to this approximation.

2.2 Mass reconstruction from weak gravitational lensing

In practice, the shear components γ_1 and γ_2 at some angular position $\boldsymbol{\theta}$ can be estimated by measuring the mean ellipticity of the galaxies at that position. This process allows one to derive the shear field as described in equation (2). Together, equation (2) with equation (6) can then be inverted to reconstruct the underlying convergence map, $\kappa(\boldsymbol{\theta})$. Kaiser & Squires (1993) proposed a method to carry out this inversion in the Fourier space:

$$\hat{\kappa} = P_1(\boldsymbol{k})\hat{\gamma}_1 + P_2(\boldsymbol{k})\hat{\gamma}_2, \quad (8)$$

where hat symbol denotes Fourier transform and

$$P_1(\boldsymbol{k}) = \frac{k_1^2 - k_2^2}{k^2}, \quad (9)$$

$$P_2(\boldsymbol{k}) = \frac{2k_1k_2}{k^2}, \quad (10)$$

where $k^2 \equiv k_1^2 + k_2^2$, and $\boldsymbol{k}$ is the Fourier counterparts for the angular coordinates $\boldsymbol{\theta}$. The inverse Fourier transform of equation (8) gives an estimate of κ. In case of an infinitely large field of view (FOV), this estimate is correct up to an overall additive constant, as constant surface mass density does not cause any shear and is thus unconstrained by γ.

The mass map κ derived in this way is unreliable due to noise caused by the limited number density of galaxies with measurable ellipticities, the finite FOV and the loss of some areas due to bright or large foreground objects. Advanced filtering techniques must be used, in particular when dealing with small fluctuations in the convergence field. In this work, we apply both the original method by Kaiser & Squires (1993) using smoothing with a Gaussian kernel, and a more advanced technique based on wavelets (see Section 4.2). Our goal is to measure κ in the best possible way at the position of HE 0435−1223 on the plane of the sky, i.e. κ_{ext} in equation (1).

2.3 E and B modes of the shear field

The validity of the reconstructed mass maps can be tested by decomposing the shear field into an 'electric' E mode and a curl or 'magnetic' B-mode map. As the shear field arises from a scalar gravitational potential, in the absence of lens–lens coupling or higher order effects, only E modes should be present in the reconstructed mass maps. Residual systematics introduced by sky subtraction or correction for the point spread function (PSF) can generate both E and B modes (e.g. Vale et al. 2004). Detection of significant B modes may therefore indicate the presence of such systematics.

The E-mode maps can be transformed into the B-mode maps by rotating the shear by 45°: $\gamma_1 \rightarrow -\gamma_2$; $\gamma_2 \rightarrow \gamma_1$. As a result, while equation (8) gives the E-mode part of the convergence map, an estimator for the B-mode convergence field is:

$$\hat{\kappa}_B = P_2(\boldsymbol{k})\hat{\gamma}_1 - P_1(\boldsymbol{k})\hat{\gamma}_2. \quad (11)$$

3 OBSERVATIONS

The imaging data for the quadruple quasar HE 0435−1223 (RA(2000) = 04^{h}38^{m}14.9^s; Dec.(2000) = −12°17′14″.4) was obtained on the 2014 March 01 with the Suprime-Cam instrument mounted on the 8.2 mSubaru telescope.[1] The strongly lensed quasar is located at the redshift of $z_s = 1.693$ (Sluse et al. 2012) and the

---

[1]Program ID: S14A-TE083; PI: C. D. Fassnacht.

lens galaxy is at the redshift of $z_l = 0.4546$ (Morgan et al. 2005; Eigenbrod et al. 2006). The reduction and calibration of the data are described in detail in H0LiCOW III. Additionally, they make use of the multiband optical and near-infrared imaging data to calculate the photometric redshifts for the galaxies. In this work, we use the deep r-band data for the weak-lensing analysis. The r-band image has a 3σ limiting magnitude of $r = 25.94 \pm 0.28$, a seeing of 0.7 arcsec, and a mean airmass of $a = 1.7$. The image is a combination of 16 exposures of 300 s each, with a pixel scale of 0.200 arcsec. The resulting useful FOV is 34 arcmin $\times$ 27 arcmin, as shown in Fig. 1.

3.1 Sky subtraction and masking

Subtracting the sky background is a critical step of the weak-lensing analysis. In the case of our data, the sky background includes imperfect illumination of the field as well as Galactic cirrus in the Southern part of the field. We subtract this foreground light contamination using the `mr_background` algorithm, which is part of the Multiresolution Analysis Software.[2] In this multiscale analysis, the background is considered to be the last scale of a pyramidal median transform (Starck et al. 1996) of the image. The number of scales is automatically calculated so that the size of the last scale is lower than or equal to $N \times N$ pixels, where N is the size of a user-specified box.

We try different last scales, i.e. the sixth, the seventh, and the eighth scales. For a 9000×9000 pixel^2 image this corresponds to $N \approx 140$, 70, and 35 pixels, respectively. We find that the seventh scale is the one that models best the spatial structures in the sky background down to the noise level, without affecting the flux of the small objects. While the sixth scale underfits the background data, i.e. leads to an overly smoothed background image, the eighth scale picks up too many fine details belonging to stars and galaxies, i.e. it overfits the data (see the bottom row of Fig. 1). The result of this background subtraction process is shown in the upper right panel of Fig. 1. We also try to remove the sky using the SEXTRACTOR software[3] (Bertin & Arnouts 1996), but the multiscale approach of the `mr_background` provides cleaner subtraction.

We apply the SEXTRACTOR software for the detection and primary measurements of galaxy and star properties. All the stars flagged as saturated by SEXTRACTOR are masked out (see Fig. 1). We apply circular masks with radius $r = 2 \times$ `FWHM_IMAGE`, where `FWHM_IMAGE` is the full width at half-maximum. We also manually mask six very bright stars with luminous haloes that extend up to 1 arcmin in radius and that are not detected by SEXTRACTOR. The radius of the masks corresponds to roughly 5σ of the Gaussian light profile of these stars, so that the mask contains almost all the flux of the saturated object.

3.2 Galaxy selection

We use all the Subaru Supreme-Cam $ugri$-band images for the star–galaxy classification and photometric redshift estimates, adopting the same techniques as in H0LiCOW III, but extending them to fainter magnitudes. The final catalogues cover the full extent of the Subaru r-band image. We keep the galaxies with photometric redshift uncertainties $\sigma_z < 0.35 \times (1 + z)$, where σ_z is the 68 per cent level errors.

---

[2] http://www.multiresolutions.com/mr/
[3] http://www.astromatic.net/software/sextractor

In order to estimate the impact of the env&los on the determination of H_0, it is necessary to measure the surface matter density κ_{ext}, projected all the way to the redshift of the quasar. Ideally, this is achieved by selecting a single plane of source galaxies at the redshift of the HE 0435−1223 quasar $z_q = 1.693$. In practice, however, such a drastic selection leads to a galaxy number density too low for adequate weak-lensing measurements. To overcome this, we select the source galaxies so that their cumulated lensing efficiency kernel is as close as possible to the kernel for a single plane at z_q, while maintaining a reasonable galaxy number density. We bin the redshifts of the source galaxies and compute the cumulated kernel as

$$\mathcal{G}(z_l) = \frac{\sum_i g(z_l, z_s^i)\, n(z_s^i)}{\sum_i n(z_s^i)}, \tag{12}$$

where $n(z_s^i)$ is the number of source galaxies per redshift bin i, z_s^i is the central source redshift of the bin, z_l is the redshift of the lens, and $g(z_l, z_s^i)$ is the lensing efficiency kernel calculated for z_s^i, i.e.

$$g(z_l, z_s^i) = \frac{4\pi G}{c^2} \frac{D_{ol} D_{ls}}{D_{os}} H(z_l - z_s^i) = \frac{H(z_l - z_s^i)}{\Sigma_{crit}}. \tag{13}$$

$H(z_l - z_s^i)$ is the Heaviside step function, which accounts for the fact that the sources in front of the structures in a given bin are not lensed. The summation is done over all redshift bins of source galaxies.

We find that selecting the source galaxies in the range $0.6 \leq z_s \leq 3.5$ (see upper panel of Fig. 2) minimizes the difference between the optimal lensing kernel at $z_s = z_q$ and the resulting cumulated one. This leaves us with a total of 12569 galaxies useful for the weak-lensing analysis, or 14 galaxies per square arcminute. The two kernels are shown in Fig. 2. While the cumulated lensing efficiency kernel is close to the ideal kernel, it does not match it perfectly. We therefore correct the effect of the mismatch between the ideal kernel and the one imposed on us by the data using N-body simulations. This last step is described in detail in Section 4.3.

Note that the uncertainties on the photometric redshifts might influence the cumulated lensing efficiency kernel. This can be tested in the following way. Instead of taking the peak of the photometric redshift estimate, for each galaxy we allocate the redshift drawn from its own redshift distribution as computed from the photo-z procedure. This changes the overall histogram shown in the upper panel of Fig. 2. We then calculate the new cumulated efficiency kernel. We repeat the procedure 1000 times, and find that the spread between the resulting curves is negligible compared to the difference between the cumulated and the ideal kernels.

4 MASS MAPPING OF THE LINE OF SIGHT TO HE 0435−1223

We produce the galaxy shape catalogue using the KSB+ software (Heymans et al. 2006), which accounts for the PSF and its spatial variations in the data. KSB+ is a refined version of an algorithm initially developed by Kaiser, Squires & Broadhurst (1995). It approximates the PSF as a small, but highly anisotropic distortion convolved with a large circularly symmetric seeing disc. KSB+ parametrizes objects according to their weighted quadruple moments and provides directly the shear estimator γ for each galaxy.

From the ellipticity catalogue, we reconstruct the shear field, accounting for edge effects and the missing data due to masking of the bright stars. We then reconstruct the convergence field using two different techniques to minimize the impact of shot noise. Finally,
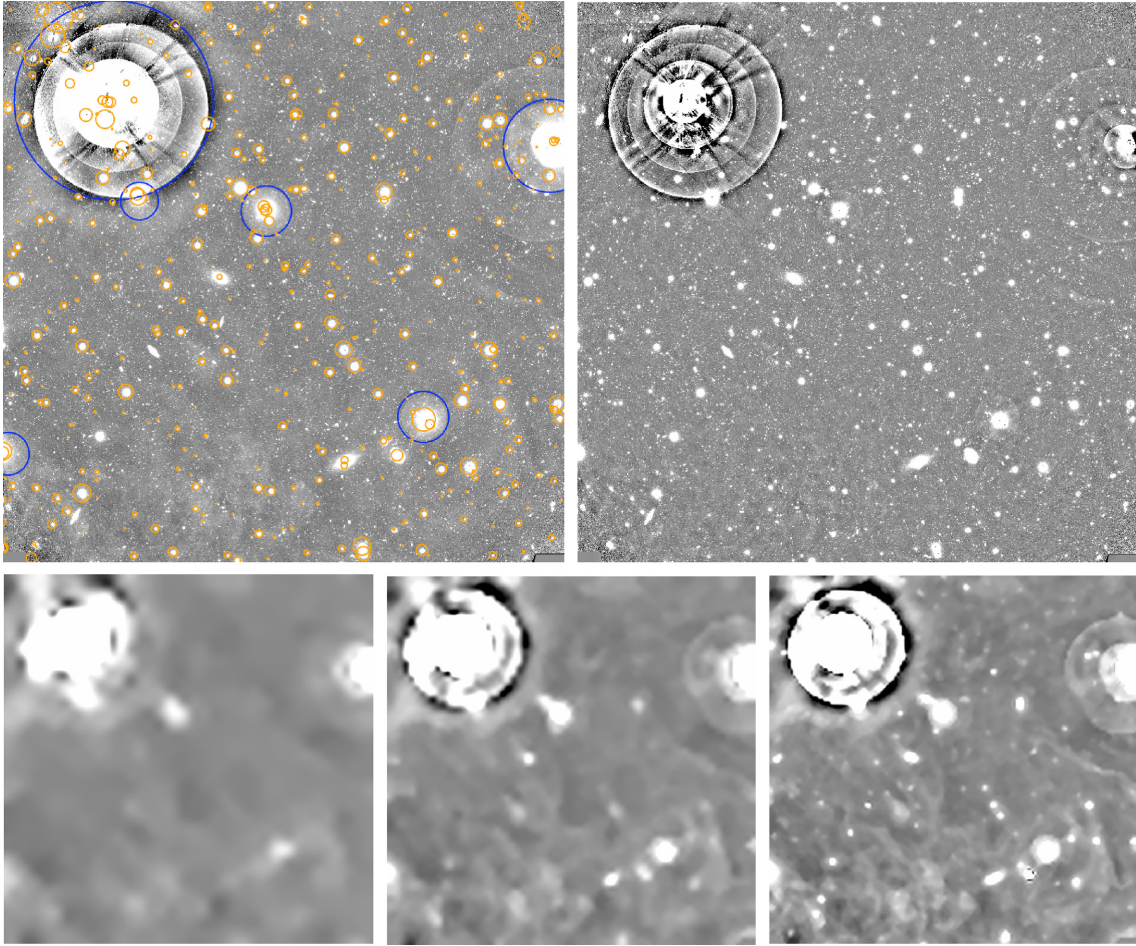
Figure 1. The $0.5° × 0.5°$ field around HE 0435−1223, with North up and East on the left. The top left panel shows the original image. The blue circles indicate the areas masked due to saturated stars, and the orange circles show the areas masked using our automated SEXTRACTOR procedure. The top right panel shows the final background-subtracted image used for the weak-lensing analysis. We show for reference different background models depending on the last scales adopted for the *mr_background* algorithm (see the text): bottom left panel – sixth scale, bottom central panel – seventh scale, and bottom right panel – eighth scale. For our analysis, we adopt the seventh scale.

we correct for the difference in the lensing efficiency kernels for our selection of galaxies and for that of a screen of background galaxies at $z = z_q$.

4.1 Reconstruction of the shear field

In order to reconstruct the convergence mass map, we make the Fourier transform of the shear field, following the equations in Section 2.2. This must be done with care, as the masks and field edges produce high-frequency signals that are aliased in the Fourier domain. To alleviate this effect, we use the FASTLENS[4] software (Pires et al. 2009a).

FASTLENS implements an inpainting algorithm, which is used to fill in the gaps in the data by extrapolating the existing information. The inpainting technique is successfully used in various astrophysical areas, e.g. CMB (Perotto et al. 2010; Plaszczynski et al. 2012; Starck, Fadili & Rassat 2013) and asteroseismology (García et al. 2014; Pires et al. 2015). The FASTLENS algorithm is set-up in the Bayesian framework, using sparsity of the solution as a prior (Elad et al. 2005). It assumes that there exists a transform dictionary,

where the complete data are more sparse than the incomplete data. In the weak-lensing case, a well-suited dictionary proves out to be the discrete cosine transform (DCT; Pires et al. 2009a). In the DCT domain, the weak-lensing signal becomes sparse, meaning that the majority of the coefficients into which the signal is decomposed turn out to be negligible. The masks introduce additional coefficients not related to the original data that can be removed by thresholding. The solution is obtained though an iterative process with exponentially decreasing thresholds, where the number of iterations is fixed empirically (Pires et al. 2009a, 2015).

When using the FASTLENS, we bin our shear map so that each spatial resolution element contains at least one galaxy. For the present data this implies the reduction of the original image size from $9000 × 9000$ to $256 × 256$ $pixels^2$, each pixel being 0.1 arcmin on a side. We perform various tests to estimate the number of iterations, that we finally fix to 300. Increasing this number does not change the result significantly. Note that, for the rest of the study, we are not using the inpainted data inside the masks. The technique is only used to avoid the artefacts produced by the aliased frequencies coming from the masks and field edges, that contaminate the signal.
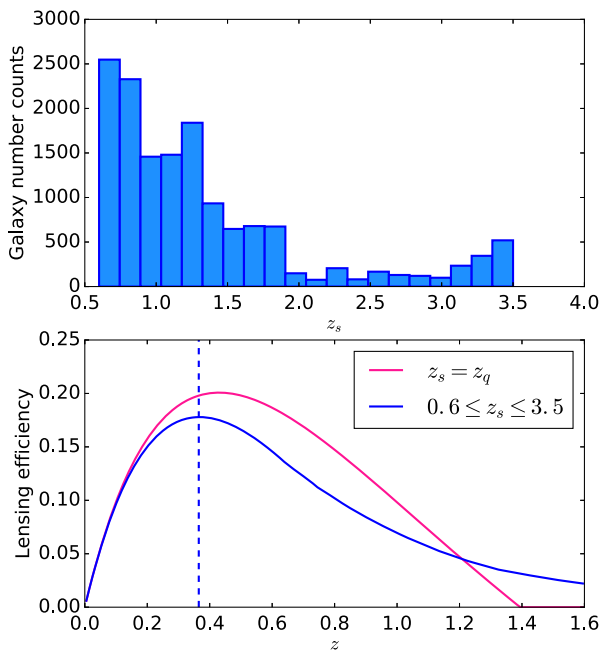
---

[4]http://www.cosmostat.org/software/fastlens/

Figure 2. The redshift distribution of the galaxies used in the weak-lensing analysis is shown on the top panel. The lower panel shows the cumulated lensing efficiency kernel computed for the selected source galaxies with $0.6 \leq z_s \leq 3.5$ (blue), as compared to the lensing efficiency kernel for the galaxies at the redshift of the lensed quasar, z_q (pink). The dashed blue line shows the lens redshift, for which the cumulated lensing efficiency is maximal.

4.2 Reconstruction of the convergence map and noise filtering

We use the standard Kaiser & Squirestechnique to convert the shear field into a convergence field (see Section2.2). The original method by Kaiser & Squires (1993) uses a Gaussian convolution kernel with varying aperture size, θ_G, to filter the data. This filtering technique is linear, easy to implement and is widely used in the field of weak lensing (e.g. Vikram et al. 2015). It has significant drawbacks, though. When large aperture sizes are used, smaller features in the map might get smoothed out, resulting in a loss of resolution. On the other hand, small θ_G values lead to larger reconstruction errors (Starck, Pires & Réfrégier 2006). Finally, the choice of θ_G itself is somewhat arbitrary.

An alternative approach to Gaussian filtering is multiscale entropy filtering (MSE; Starck & Murtagh 2006), successfully used in different applications of weak lensing (e.g. Pires et al. 2009b; Lin, Kilbinger & Pires 2016). MSE filtering is a non-linear Bayesian filtering technique which uses an MSE prior.

The data are decomposed into multiple scales using the 'à trous' wavelet transform (Holschneider et al. 1989). This transform ensures the sparsity of the lensing signal at all spatial scales. Importantly, the noise in this dictionary is non-sparse, while the lensing signal is. As a consequence, most of the lensing information is described by few highly significant coefficients, while the noise is spread over many non-significant coefficients. These are removed using the false discovery rate (Benjamini & Hochberg 1995; Miller et al. 2001), which adapts the selection threshold based on the desired fraction of false detections over the total number of detections.

The MSE prior is constructed using all the non-significant coefficients in each of the wavelet scales. The entropy is calculated by modelling the noise in the data (Starck et al. 2001), which produces

good results for the analysis of piecewise smooth images and is thus well adapted for the mass reconstruction (Starck et al. 2006).

We apply both Gaussian and the MSE filtering techniques to the images of HE 0435−1223. For the Gaussian filtering, we adopt two different kernel apertures: $\theta_G = 0.5$ and 1 arcmin, which allow us to achieve a fairly good spatial resolution, while still preserving the Gaussian properties of the noise (e.g. van Waerbeke 2000). For the MSE filtering, we use the MSE algorithm implemented in the MRLENS[5] software (Starck et al. 2006). We decompose the original image into six wavelet scales, and filter the first five scales, starting from the highest spatial frequencies. We specify the fraction of false detections to be $\alpha = 0.01$ (1 per cent) for the first scale, which roughly corresponds to a 3σ thresholding (Miller et al. 2001), where σ is the noise standard deviation. This fraction is gradually decreased by a factor of 2 for every subsequent scale.

4.3 Correcting for the lensing efficiency

Our selection of galaxies, which maximizes the number density of measurable sources, yields an effective lensing efficiency kernel which is somewhat different from the ideal one where all source galaxies lie at the redshift of the quasar $z_s = z_q$. What we measure from our data **d** is thus $P(\kappa_{wl}|\mathbf{d})$. To account for possible resulting misestimation of the external convergence, we calibrate our measurement using ray tracing through the MS. In this way, we estimate $P(\kappa_{ext}|\mathbf{d})$, which is the final result of this analysis.

The MS (Springel et al. 2005) is a large high-resolution cosmological simulation, run with GADGET-2 code (Springel 2005) assuming the ΛCDM model of hierarchical structure formation. It follows the evolution of $N = 2160^3$ dark matter particles with masses of $8.6 \times 10^8 h^{-1} M_\odot$ from redshift $z = 127$ to 0 in a cubic region with comoving side length $L = 500 h^{-1}$ Mpc. The resulting MS dark matter haloes are then populated with galaxies using the semi-analytic galaxy models by De Lucia & Blaizot (2007).

Hilbert et al. (2009b) estimated the lensing effect produced by the dark matter structures of the MS using the ray-tracing algorithm based on the multiple-lens–plane approximation. This multiple-lens–plane approximation allows us to calculate lensing observables by projecting the continuous mass distribution on discrete lens planes with an accuracy of a few percent. Hilbert et al. (2008) took into account the additional effects of luminous matter from galaxies with stellar masses $\geq 10^9 h^{-1} M_\odot$, which were taken from the catalogue by De Lucia & Blaizot (2007).

We select 1024 fields from the MS with the FOV of $0.5° \times 0.5°$, which we populate with our source galaxies, preserving their position in the 3D space (RA, Dec., z_{phot}). Following Hilbert et al. (2008, 2009b), we perform the multiple-lens–plane ray tracing to calculate the shear for all source galaxies. For each of 1024 fields, we generate 1000 noisy realizations by adding the shape noise, which is drawn from a normal distribution with $\sigma_\gamma = 0.25$, as estimated from the data. We then apply our mass map reconstruction and noise filtering methods on these simulated fields to measure the weak-lensing convergence maps κ_{wl}^{MS}.

Using the same ray-tracing technique, we calculate the shear for the source galaxies at (RA, Dec., z_q), i.e. maintaining their 2D position, but placing them all at the redshift of the quasar z_q. After performing the reconstruction, we produce κ_{ext}^{MS} maps for the case of the ideal kernel, i.e. with all source galaxies lying at the same redshift.

[5] http://www.cosmostat.org/software/mrlens/

The simulations we carry out provide $P(\kappa_{ext}^{MS}, \kappa_{wl}^{MS})$ for all three filtering techniques, as shown in Fig. 3. We define κ_{ext} as the corrected external convergence that has all the sources located at the quasar redshift. We can obtain κ_{ext} from the κ_{wl} that we measure from the data using our pipeline by identifying κ_{wl}^{MS} with κ_{wl} and κ_{ext}^{MS} with κ_{ext}, such that

$$P(\kappa_{ext}|\kappa_{wl}) = P(\kappa_{ext}^{MS}|\kappa_{wl}^{MS}). \tag{14}$$

The probability density function (PDF) of κ_{ext} given the available data $\mathbf{d}$, i.e. $P(\kappa_{ext}|\mathbf{d})$, is then

$$P(\kappa_{ext}|\boldsymbol{d}) = \int d\kappa_{wl}\ P(\kappa_{ext}|\kappa_{wl}) \times P(\kappa_{wl}|\boldsymbol{d}). \tag{15}$$

5 LINE-OF-SIGHT CONVERGENCE

Fig. 4 shows our measured convergence maps for HE 0435−1223, produced using the data described in Section 3 and the analysis pipeline detailed in Section 4. The maps are given for each of the three filtering techniques and for both E and B modes, prior to the correction described in Section 4.3. As lensing does not produce B modes, the corresponding map should not show any significant B-mode signal. This is the case for our data according to the right-hand column of Fig. 4.

To quantify this further, we estimate the statistical uncertainties by rotating the galaxies by a random angle, preserving their initial shapes and positions. We generate 1000 such shear fields, which we analyse with our pipeline to produce 1000 corresponding κ_E and κ_B maps for each filtering technique. The standard deviation between these 1000 maps provides a corresponding noise map, which contains the galaxy shape noise and the measurement error. We then divide the original maps by the noise maps to estimate the signal-to-noise ratio (S/N) of the structures.

From these S/N maps, we generate the S/N distributions for the E and the B modes. In the absence of the signal, the B modes should be consistent with a normal distribution centred at zero with a standard deviation equal to one. The S/N distribution of the E modes should, on the contrary, have a standard deviation greater that one (e.g. Utsumi et al. 2014). Our results are displayed in Fig. 5, where indeed the B modes agree with Gaussian distribution for all three filtering techniques. The E modes deviate from Gaussian distribution, which is indicative of a lensing signal. The standard deviation of the E-mode distributions is 1.4 for the MSE and 1 arcmin Gaussian filtering, and 1.2 for the 0.5 arcmin Gaussian filtering. Our mock simulations described in Section 6 show that the same signal can be produced by a halo with $M_{vir} = 6 \times 10^{14} h^{-1} M_{\odot}$.

Finally, to estimate the external convergence along the line of sight to the HE 0435−1223 system, we measure the convergence inside the central pixel of our mass maps. We use the 1000 noise realizations to construct $P(\kappa_{wl}|\mathbf{d})$ for each noise filtering method, which we centre on the values obtained from the corresponding signal maps. We then correct the PDFs for the difference in the lensing efficiency kernel, by weighting them with the joint distributions obtained from the MS, as described in Section 4.3, which yields $P(\kappa_{ext}|\mathbf{d})$. This correction also accounts for the smaller scales, possibly omitted in our analysis due to the noise filtering. Our final $P(\kappa_{ext}|\mathbf{d})$ are displayed in Fig. 6, together with the results from H0LiCOW III based on weighted galaxy counts. The values of κ_{ext} at the position of HE 0435−1223 and associated error bars are given in Table 1.

5.1 Comparison with the results from H0LiCOW III

We now investigate the consistency between the weak lensing ($\kappa_{ext}^{wl} \equiv \kappa^{wl}$, this paper) and weighted number counts ($\kappa_{ext}^{nc} \equiv \kappa^{nc}$, H0LiCOW III) techniques. To do so, we adopt the Bayesian formalism proposed in Marshall, Rajguru & Slosar (2006) and we test two hypotheses:

(i) H^{global}: both results can be consistently explained within one set of cosmological parameters, describing the same field and environment.

(ii) H^{ind}: there are some unaccounted systematic errors leading to an offset, which can be parametrized with a second independent set of cosmological parameters. In this case, two sets of parameters are needed to account for the two results separately, as they are describing two different environments.

To infer which hypothesis is favoured by the data, we calculate the Bayes factor F, given by

$$F = \frac{P(\kappa^{wl}, \kappa^{nc}|H^{global})}{P(\kappa^{wl}, \kappa^{nc}|H^{ind})}. \tag{16}$$

In our case, this reduces to

$$F = \frac{\langle L^{wl} L^{nc} \rangle}{\langle L^{wl} \rangle \langle L^{nc} \rangle}, \tag{17}$$

where L^{wl} and L^{nc} are, respectively, the likelihoods of an external convergence obtained from the weak lensing and from the weighted number count methods (see the appendix in Suyu et al. (2013) for the derivation of the formula). If $F > 1$, the data favour hypothesis H^{global} describing the same environment.

The values for the Bayes factor F for three filtering techniques are given in Table 1. For reference, two 1D Gaussian likelihoods have a Bayes factor of $F = 1$ if they overlap within 2σ's, and $F \sim 3.6$ if the two distributions overlap within 1σ. As in our case, all Bayes factors are noticeably larger than 1, we conclude that the convergence estimates by the weak-lensing technique and by the weighted galaxy number count technique provide consistent results. We also see that the MSE noise filtering technique that preserves the best the smaller scales is more in agreement with the weighted galaxy number count technique. The Gaussian filtering with $\theta_G = 1$ arcmin is the least consistent, probably as it washes out the information on smaller scales, which is important for the local estimation of the external convergence. Note that the difference between the H0LiCOW III and our results for all three filtering techniques is considerably smaller than the final uncertainty on H_0 for the HE 0435−1223 system alone, as quoted by Bonvin et al. (2017).

To further check the consistency, we use our final results for external convergence to compute the Hubble parameter H_0 for the HE 0435−1223 system. The PDF's for H_0 are shown in Fig. 7. For the MSE filtering, the median position shifts from $H_0 = 73.1$ km s^{-1} Mpc^{-1} for galaxy number counts technique to $H_0 = 74.3$ km s^{-1} Mpc^{-1}, which is fully consistent within the error bars.

6 TESTING THE PRESENCE OF A MASSIVE HALO IN THE VICINITY OF THE LENSING GALAXY

The lensing galaxy in HE 0435−1223 is part of a group of galaxies (e.g. Sluse et al. 2017), which we do not detect in our weak-lensing maps. In order to test the significance of this non-detection, and to
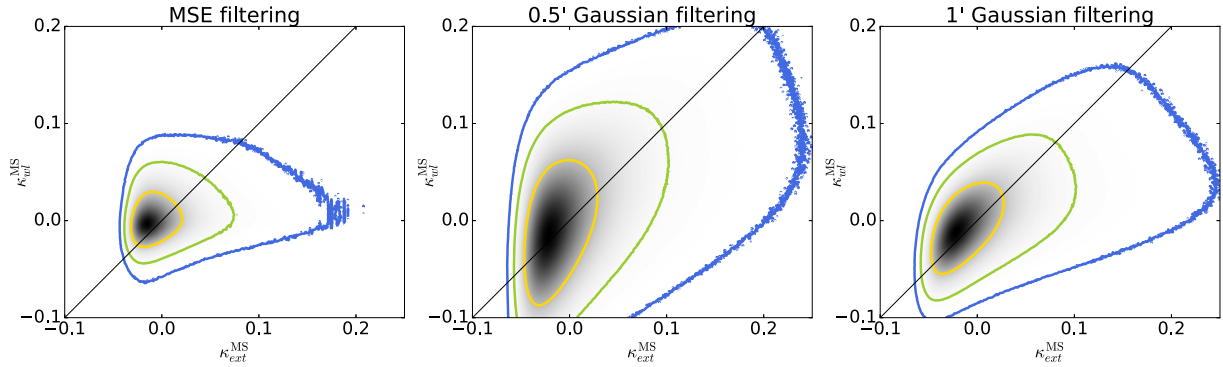
Figure 3. Joint distributions for the convergence inferred from the MS for the sources following our observed redshift distribution, i.e. κ_{ext}^{MS}, and for the sources lying in a single-redshift plane, i.e. κ_{ext}^{MS}. The left-hand panel corresponds to the MSE filtering of the data, the middle panel to the Gaussian filtering with $\theta_G = 0.5$ arcmin, and the right-hand panel to the Gaussian filtering with $\theta_G = 1$ arcmin. The yellow, green, and blue contours show the 1σ, 2σ, and 3σ regions, respectively. The black line indicates the perfect correlation.
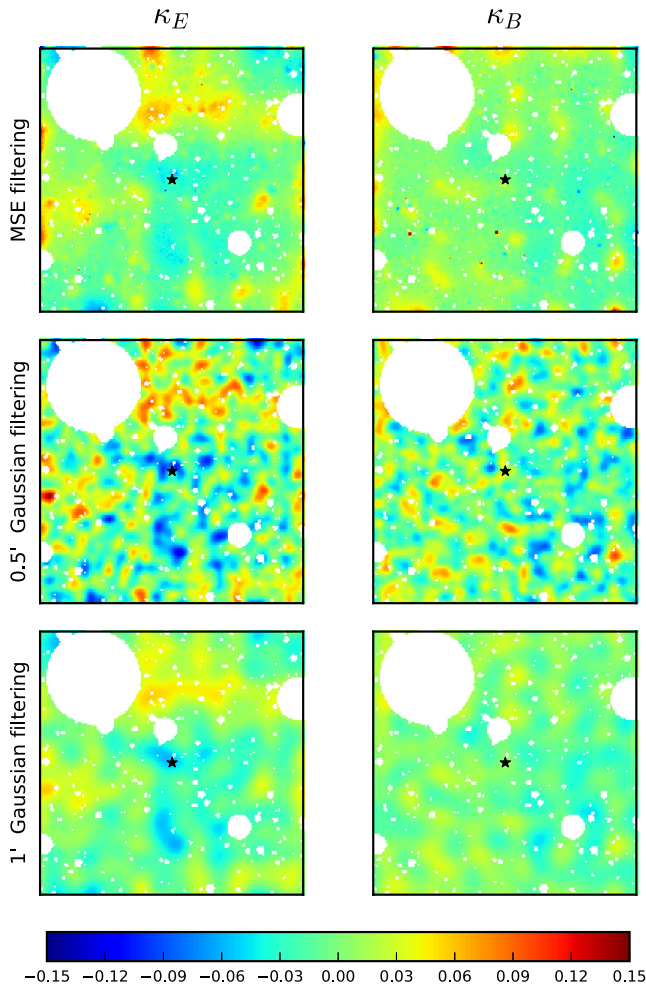
Figure 4. Convergence maps for the $0.5° \times 0.5°$ field around HE 0435−1223, indicated by a star in the centre. The left-hand column shows the E modes and the right-hand column the B modes. The upper row corresponds to the MSE filtering of the data, the middle row to the Gaussian filtering with $\theta_G = 0.5$ arcmin, and the bottom row to the Gaussian filtering with $\theta_G = 1$ arcmin. All maps have pixel scale of 0.1 arcmin. The white regions correspond to masked stars and bright foreground objects.

assess the sensitivity of our mass reconstruction technique to individual haloes, we perform weak-lensing simulations. We simulate the shear produced by a massive halo in the vicinity of the lens and build images that mimic the data using GALSIM[6] (Rowe et al. 2015). We then run our pipeline to see whether we can recover the halo injected in the image.

6.1 Injecting a simulated halo in the data

The recipe we use to construct the simulated data can be summarized as follows.

(i) *Field of view:* we set the FOV to $0.5 \times 0.5 \deg^2$ with a pixel size of 0.2 arcsec to mimic the HE 0435−1223 field. The geometry of all masks is preserved;

(ii) *PSF:* for simplicity, we assume a Gaussian PSF with a fixed width that matches the median width of all stars in the FOV, i.e. FWHM = 0.7 arcsec;

(iii) *Galaxy population:* we leave the galaxy population the same as in the real data, i.e. with the same ellipticities, photometric and geometric properties, the same positions on the sky, and the same photometric redshifts;

(iv) *Massive halo:* not all structures around the lensed quasar influence the H_0 measurements equally. In general, galaxies that lie within 1 arcmin radius in projection along the line of sight tend to affect H_0 more (e.g. McCully et al. 2017b). Similarly, structures in the foreground of the lens tend to have higher impact, while other perturbers influence H_0 only at the subpercent level. Given this and the specific cumulative lensing efficiency kernel for our source galaxies, we simulate the external convergence produced by a Navarro–Frenk–White (NFW) halo (Navarro, Frenk & White 1997) at redshift $z_{halo} = 0.37$. This redshift is in the foreground of the lens and corresponds to the maximum of the cumulated efficiency kernel for our selection of source galaxies. Placing the halo at the redshift of the lens would decrease the lensing efficiency, although making the halo physically related to the lens. Our simulations and tests therefore give the minimal mass necessary to see the lensing signal at redshift $z_{halo} = 0.37$. A halo at any other redshift would have to be more massive in order to be detected by our pipeline.

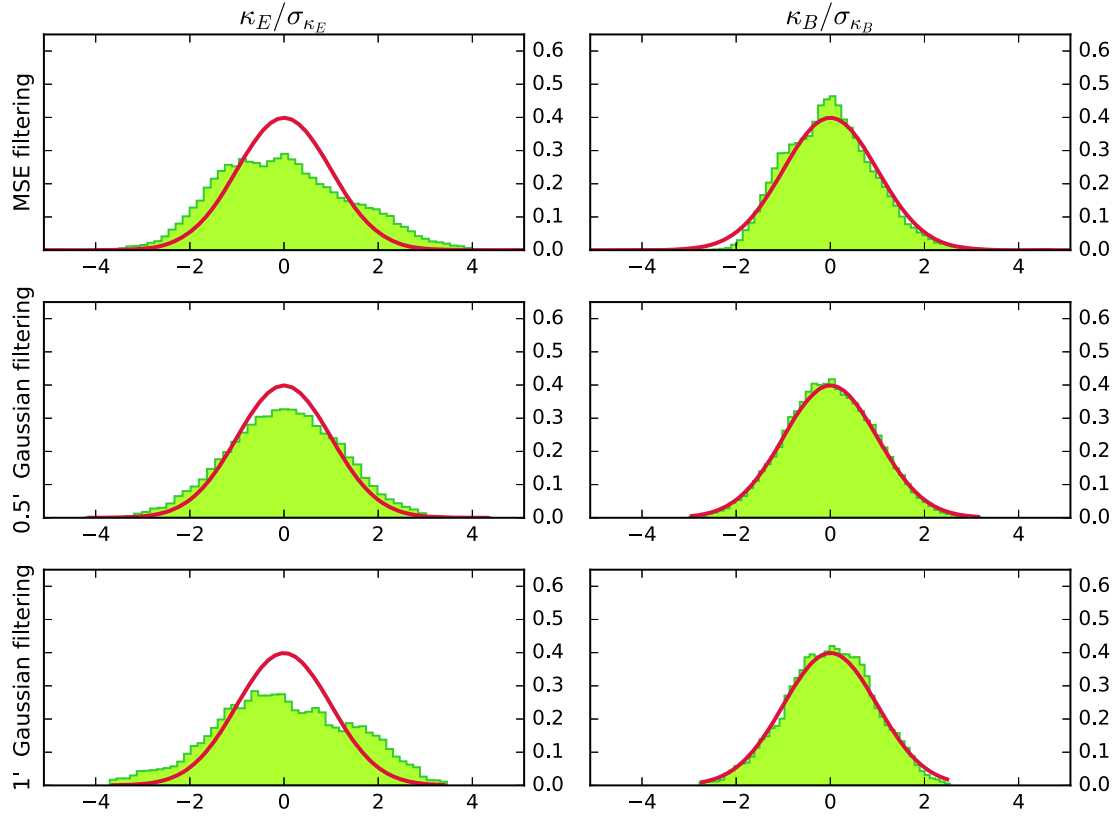[6]https://github.com/GalSim-developers/GalSim

Figure 5. Normalized S/N distributions of convergence maps with E modes shown on the left and the B modes on the right. From top to bottom are shown the MSE filtering, and the Gaussian filtering with $\theta_G = 0.5$ and 1 arcmin. In each panel, the solid line shows a normal distribution centred at zero with a unit standard deviation. The B modes are compatible with a normal distribution for all filtering techniques, while E modes deviate significantly, as expected in the presence of a weak-lensing signal.
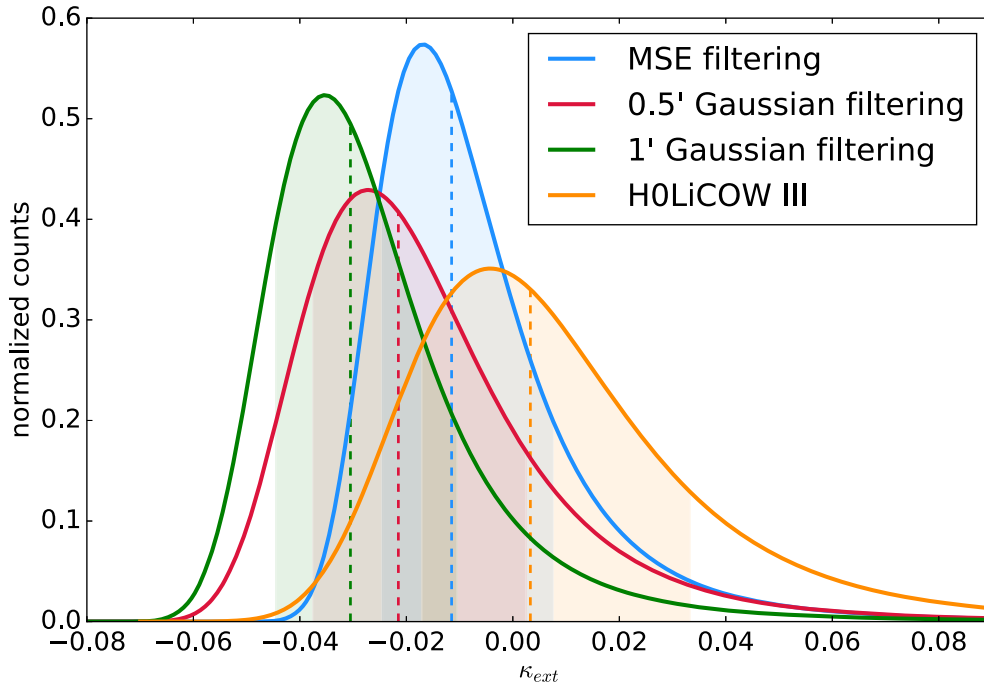

Figure 6. PDFs of external convergence for the HE 0435−1223 field. The blue distribution corresponds to the MSE filtering of the data, red to the Gaussian filtering with $\theta_G = 0.5$ arcmin, and green to the Gaussian filtering with $\theta_G = 1$ arcmin. The orange distribution shows the result from H0LiCOW III. Dashed lines show the values at the 50 per cent percentile. Shaded regions indicate the 1σ regions.

Table 1. External convergence estimates for the HE 0435−1223 field using three different noise filtering techniques: MSE filtering, Gaussian filtering with $\theta_G = 0.5$ and 1 arcmin. The values are given at the position of the quasar. For the comparison, we also give the values from H0LiCOW III. κ_{ext} show median value, σ_κ^- and σ_κ^+ correspond to deviation from 16th and 84th quantiles, respectively. For each of the filtering techniques, we indicate the Bayes factor calculated with respect to the H0LiCOW III result (see the text).

Filtering technique	κ_{ext}	σ_κ^-	σ_κ^+	F
MSE	−0.012	0.013	0.020	5.1
G0.5′	−0.022	0.016	0.025	3.7
G1′	−0.031	0.014	0.040	2.7
H0LiCOW III	0.003	0.020	0.030	–
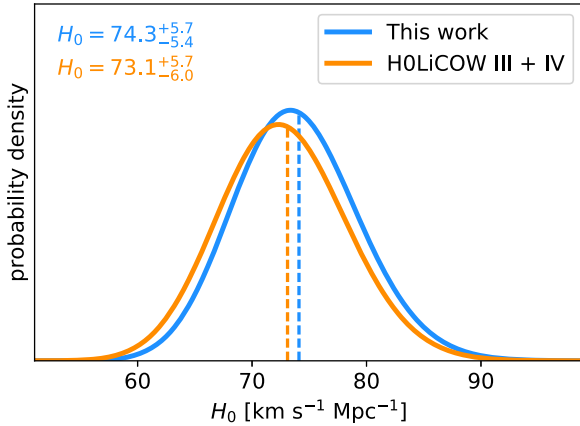
Figure 7. Marginalized posterior probability distributions for H_0 in the framework of the ΛCDM cosmology. External convergence is computed using galaxy number counts technique for the blue line, and the weak-lensing technique for the orange line. Two distributions are fully compatible within the error bars.

(v) *Shear field:* we calculate the shear values for the simulated NFW halo at the position of all background galaxies. We use GALSIM to apply the shear to the corresponding sources;

(vi) *Noise:* we add Gaussian distributed noise to the simulated field, with the same mean standard deviation as the original data.

Assuming a mass–concentration relation, the NFW profile can be described using only two free parameters: the virial mass M_{vir} and the redshift z_{halo} (Takada & Jain 2003). We are using the mass–concentration relation from Duffy et al. (2008) in the form

$$c(z, M_{\text{vir}}) = A(M_{\text{vir}}/M_{\text{pivot}})^B (1 + z)^C, \qquad (18)$$

where in case of the relaxed halo $M_{\text{pivot}} = 10^{12} h^{-1} M_\odot$, $A = 6.71$, $B = -0.091$, and $C = -0.44$. We adopt the definition of the virial mass as the total mass within a circular area in which the mean internal density is 200 times the critical density.

To assess the sensitivity of our pipeline, we simulate 10 haloes within a mass range $13.8 < \log M_{\text{vir}}[h^{-1} M_\odot] < 15.0$. For each halo, we generate 1000 fields, where we randomize the orientation of the background galaxies before applying the corresponding shear calculated by GALSIM. This is necessary to cancel out any shear signal present in the data and not due to the simulated halo. Drawing 1000 simulations allows us to estimate the statistical error bars.

We apply the pipeline described in Section 4 to every simulated field. We first measure the shear field using the KSB, and then build the corresponding convergence maps using the Kaiser & Squires in-
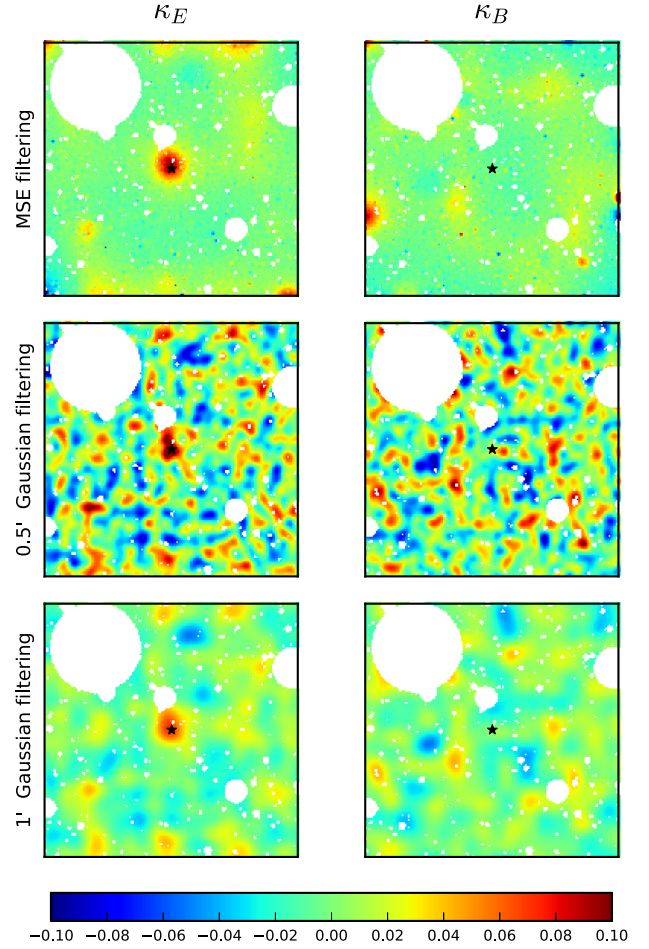

Figure 8. Convergence maps of the simulated $0.5° \times 0.5°$ field containing an NFW halo with virial mass $\log M_{\text{vir}} = 14.5 h^{-1} M_\odot$. Such a halo is well detected in the E-mode map but, as expected, does not show up in the B modes. All panels are the same as in Fig. 4.

version, the FASTLENS and the MRLENS multiresolution algorithms. An example of mass reconstruction done on one of the simulated fields is given in Fig. 8.

6.2 Halo detection

We now test how well we can recover the structures injected in the field simulations. A natural way to detect peaks is by setting a threshold on the S/N ratio for the possible detections in each of the 1000 mocks. For the sake of comparison, we follow two different approaches. The first is based on the S/N of the peaks. We estimate the noise by taking the standard deviation of the 1000 realizations for each halo. To check if there is a halo, we calculate the S/N of the nine central pixels and set the threshold to $S/N_9 = 5$. The second approach is based on the standard deviation of the noise in the fields. We sum the convergence inside the nine central pixels, i.e. $\Sigma\kappa_9$, and compare this value to the standard deviation σ_κ in the regions of the field that do not contain any signal from the halo. We set the criterion to $\Sigma\kappa_9 > 5\sigma_\kappa$.

According to the central limit theorem, a Gaussian smoothing produces Gaussian noise if the number of galaxies inside the smoothing window is on average 10 or larger (e.g. van Waerbeke 2000). With a galaxy density of 14 galaxies per square arcminute,
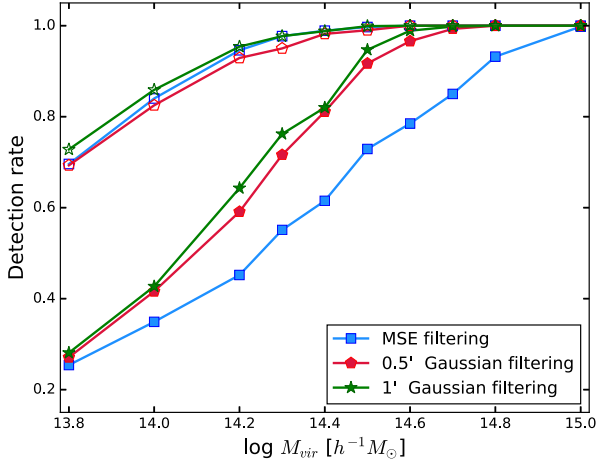
Figure 9. Detection rates of haloes in the 1000 simulated fields. Filled symbols show the selection based on the S/N ratio of the haloes. Open symbols show the selection based on the standard deviation of the noise in the convergence field. The colour code indicates the three filtering techniques.

Table 2. Virial mass, associated uncertainty, and radius of the spectroscopic groups in the field of HE 0435−1223 identified in Sluse et al. (2017). The last column shows our weak-lensing detection limit in terms of virial mass for haloes at each of the group redshifts. The limit is obtained according to equation (19).

$\bar{z}_{group}$	$\log(M_{vir}/M_\odot)$	R_{vir} (Mpc)	$\log(M_{vir}/M_\odot)_{limit}$
0.0503	13.32 ± 0.61	0.635	15.52
0.1744	13.81 ± 0.40	1.071	14.57
0.1841	13.65 ± 0.46	0.954	14.57
0.3202	13.83 ± 0.36	1.259	14.37
0.4185	13.18 ± 0.48	0.873	14.37
0.4547	13.72 ± 0.36	1.385	14.42
0.5059	13.72 ± 0.36	1.373	14.42
0.5650	13.33 ± 0.43	0.971	14.52
0.7019	12.49 ± 0.63	0.654	14.72

this criterion is satisfied for both the 0.5 and 1 arcmin Gaussian filtering. The MSE filtering, on the other hand, is a non-linear multiscale technique, which results in the highly non-Gaussian noise (e.g. Jiao, Shan & Fan 2011; Lin, Kilbinger & Pires 2016). Thus, note that for both approaches the results for MSE filtering have to be interpreted and compared with caution, as the actual underlying statistics are non-Gaussian. However, in our case of the low S/N of the lensing signal, deviation from Gaussian statistics is not significant.

Fig. 9 shows the fraction of fields with detected haloes as a function of virial mass. As expected, this fraction tends to zero for low-mass haloes, and to 100 per cent for the high-mass end of the distribution. It is important to note that this distribution depends on the halo selection technique, with the approach based on the S/N of the peaks giving more pessimistic results. Following this approach, we are able to identify an NFW halo of $M_{vir} = 1.6 \times 10^{14} h^{-1} M_\odot$ with a detection probability in the range $45 - 65$ per cent, depending on noise filtering technique. We consider this halo mass our detection limit at the redshift $z_{halo} = 0.37$, which corresponds to the maximum of the cumulated lensing efficiency kernel, as illustrated in Fig. 2.

For a known source redshift distribution, weak-lensing convergence depends on the redshift of the halo. Using the cumulated lensing efficiency kernel for our source galaxy population (see Fig. 2, lower panel), we can rescale the convergence to match the weak-lensing detection limit for other redshifts:

$$\kappa(z_l) = \frac{\mathcal{G}(z_l)}{\mathcal{G}(z_l = 0.37)} \kappa(z_l = 0.37). \qquad (19)$$

The new convergence $\kappa(z_l)$ then corresponds to the virial mass of a halo at redshift z_l. We calculate the limiting masses for the haloes at the redshifts, where Sluse et al. (2017) find spectroscopic groups in the field of HE 0435−1223. Following Table 2, the virial masses of all these groups are marginally below our detection limit. Wilson et al. (2016, 2017) estimate the virial mass of the group at redshift $z \approx 0.18$ to be higher than that of Sluse et al. (2017), but as its mass given the error bars equals our detection limit, we cannot discriminate between the two results. We can still confirm, however, that there are no structures in the field of HE 0435−1223

more massive than our detection limits, in agreement with Sluse et al. (2017).

Depending on their mass, position, and redshift, structures present in the field of the lensed quasar can be either approximated as external convergence, or need to be explicitly taken into account during the lens modelling for the unbiased estimate of H_0. In order to assess the significance of our detection limit, we estimate when a halo with $M_{vir} = 1.6 \times 10^{14} h^{-1} M_\odot$ at the redshift of $z_{halo} = 0.37$ falls into the first case. We adopt the diagnostic proposed by McCully et al. (2017a) and calculate the quantity called 'flexion shift' $\Delta_3 x$. It is used by Sluse et al. (2017) in order to estimate which galaxies in the field of HE 0435−1223 need to be directly included in the modelling of the lens system in Wong et al. (2017) as they would reveal themselves by inducing a noticeable shear and flexion, and which can be adequately described by the external shear.

$\Delta_3 x$ characterizes how the positions of lensed quasar images are perturbed in the presence of the mass external to the main lens. If the external perturber is assumed to be a point mass, the flexion shift given in arcseconds is

$$\Delta_3 x = \frac{\theta_d^2 \theta_p^2}{\Delta \theta_{dp}^3} \times f(\beta), \qquad (20)$$

where θ_d and θ_p are the Einstein radii of the main deflector and the external perturber, respectively, $\Delta \theta_{dp}$ is the angular separation on the sky between the deflector and the perturber, and

$$f(\beta) = \begin{cases} 1 & \text{for } z_p < z_d \\ (1-\beta)^2 & \text{for } z_p > z_d, \end{cases} \qquad (21)$$

where z_d and z_p are the redshifts of the deflector and the perturber, respectively, and β is the combination of angular diameter distances:

$$\beta = \frac{D_{dp} D_{os}}{D_{op} D_{ds}}. \qquad (22)$$

McCully et al. (2017a) showed, that in order to avoid bias on H_0 at the percent level, perturbers with flexion shift $\Delta_3 x > 10^{-4}$ need to be included explicitly in the lens modelling, while ones with $\Delta_3 x < 10^{-4}$ can be treated as external convergence. We thus use $\Delta_3 x = 10^{-4}$ as the limit criterion.

For perturber with mass $M = 1.6 \times 10^{14} h^{-1} M_\odot$ at the redshift of $z_{halo} = 0.37$, the Einstein radius is $\theta_p = 35.02$ arcsec. The Einstein radius of the HE 0435−1223 lens is $\theta_d = 1.182$ arcsec (Wong et al. 2017). We therefore obtain that the minimal necessary separation between the main lens and the perturber, so that the latter is treated as tidal perturbation, is $\theta = 4.3$ arcmin. If NFW halo is placed at this distance from the lens, the convergence at the position of

the quasar is $\kappa = 0.008$. According to equation (1), this means that our detection limit places a potential systematic bias on H_0 of < 1 per cent.

7 SUMMARY

We characterize the effects of the env&los in the field of the gravitationally lensed quasar HE 0435−1223. We give a weak-lensing estimation of the external convergence κ_{ext}, using the deep Subaru Suprime-Cam images and the photometric redshift catalogues from H0LiCOW III. The weak-lensing measurements are carried out on a final catalogue containing 14 galaxies per square arcminute. The resulting shear field is processed with the inpainting technique to optimally account for border effects and masks of the regions affected by bright stars or extended foreground objects.

After applying the inversion, we filter the resulting noisy convergence map in three different ways: using MSE and smoothing with 0.5 and 1 arcmin Gaussian kernels. The statistical errors are estimated using realistic mocks of the data and the systematic errors are checked by decomposing the mass maps into E and B modes, showing that our statistical errors dominate the systematics.

Our main result is the PDF for the external convergence inside the central pixel, i.e. at the position of the HE 0435−1223 (see Fig. 6 and Table 1). We find that the HE 0435−1223 env&los is marginally underdense (compared to the rest of the Universe) with a convergence being slightly negative. Our estimates are also compatible with the zero external convergence, as is found in H0LiCOW III based on weighted galaxy number counts. Since the weak gravitational lensing measurements do not depend on assumptions about the correlation between light and mass distributions along the line of sight, our result is independent of and complementary to H0LiCOW III.

We test the possibility that the lensing galaxy of HE 0435−1223 is perturbed by a single massive halo close to the lens. From the image simulations with fake haloes, we show that our detection limit in mass is $M_{vir} = 1.6 \times 10^{14} h^{-1} M_\odot$ at the redshift $z_{halo} = 0.37$, which corresponds to the maximum of the cumulated lensing efficiency kernel. We scale this result according to the cumulated lensing efficiency kernel of our source galaxies in order to deduce the limit for other halo redshifts. Since we do not detect any halo in the real data, this supports the result of Sluse et al. (2017), who estimates that the virial masses of all spectroscopic groups in the field of HE 0435−1223 are lower than $M_{vir} = 1.6 \times 10^{14} h^{-1} M_\odot$. We also note that our detection limit places a potential bias on the estimate of H_0 of order of < 1 per cent.

To summarize, our work supports the finding by H0LiCOW III that the cosmology results for the HE 0435−1223 system alone in Bonvin et al. (2017) are not significantly affected by line-of-sight effects.

REFERENCES

Abbott B. P. et al., 2017, Nature, 551, 85
Alam S. et al., 2017, MNRAS, 470, 2617
Auger M. W., Fassnacht C. D., Abrahamse A. L., Lubin L. M., Squires G. K., 2007, AJ, 134, 668
Bartelmann M., Schneider P., 2001, Phys. Rep., 340, 291
Benjamini Y., Hochberg Y., 1995, J. R. Stat. Soc. B, 57, 289
Bertin E., Arnouts S., 1996, A&AS, 117, 393
Birrer S., Welschen C., Amara A., Refregier A., 2017, J. Cosmol. Astropart. Phys., 4, 049
Bonvin V., Tewes M., Courbin F., Kuntzer T., Sluse D., Meylan G., 2016, A&A, 585, A88
Bonvin V. et al., 2017, MNRAS, 465, 4914
Coe D., Moustakas L. A., 2009, ApJ, 706, 45
Collett T. E., Cunnington S. D., 2016, MNRAS, 462, 3255
Collett T. E. et al., 2013, MNRAS, 432, 679
Courbin F., Eigenbrod A., Vuissoz C., Meylan G., Magain P., 2005, in Mellier Y., Meylan G., eds, IAU Symp. Vol. 225, Gravitational Lensing Impact on Cosmology, Cambridge Univ. Press, Cambridge. p. 297
Courbin F. et al., 2011, A&A, 536, A53
De Lucia G., Blaizot J., 2007, MNRAS, 375, 2
DES Collaboration et al., 2017, preprint (arXiv:1711.00403)
Ding X. et al., 2017a, MNRAS, 465, 4634
Ding X. et al., 2017b, MNRAS, 472, 90
Duffy A. R., Schaye J., Kay S. T., Dalla Vecchia C., 2008, MNRAS, 390, L64
Eigenbrod A., Courbin F., Meylan G., Vuissoz C., Magain P., 2006, A&A, 451, 759
Elad M., Starck J.-L., Querre P., Donoho D., 2005, J. Appl. Comput. Harmon. Anal., 19, 340
Fadely R., Keeton C. R., Nakajima R., Bernstein G. M., 2010, ApJ, 711, 246
Falco E. E., Gorenstein M. V., Shapiro I. I., 1985, ApJ, 289, L1
Fassnacht C. D., Xanthopoulos E., Koopmans L. V. E., Rusin D., 2002, ApJ, 581, 823
Fassnacht C. D., Gal R. R., Lubin L. M., McKean J. P., Squires G. K., Readhead A. C. S., 2006, ApJ, 642, 30
Fassnacht C. D., Koopmans L. V. E., Wong K. C., 2011, MNRAS, 410, 2167
Fernández Arenas D. et al., 2018, MNRAS, 474, 1250
Fischer P., Bernstein G., Rhee G., Tyson J. A., 1997, AJ, 113, 521
Freedman W. L., Madore B. F., Scowcroft V., Burns C., Monson A., Persson S. E., Seibert M., Rigby J., 2012, ApJ, 758, 24
García R. A. et al., 2014, A&A, 568, A10
Goobar A. et al., 2017, Science, 356, 291
Greene Z. S. et al., 2013, ApJ, 768, 39
Heymans C. et al., 2006, MNRAS, 368, 1323
Hilbert S., White S. D. M., Hartlap J., Schneider P., 2008, MNRAS, 386, 1845
Hilbert S., Hartlap J., White S. D. M., Schneider P., 2009a, A&A, 499, 31
Hilbert S., Hartlap J., White S. D. M., Schneider P., 2009b, A&A, 499, 31
Holschneider M., Kronland-Martinet R., Morlet J., Tchamitchian P., 1989, in Combes J.-M., Grossmann A., Tchamitchian P., eds, Wavelets. Time-Frequency Methods and Phase Space, Springer-Verlag, Berlin. p. 286
Jaroszyński M., Skowron J., 2016, MNRAS, 462, 1405
Jiao Y.-X., Shan H.-Y., Fan Z.-H., 2011, Res. Astron. Astrophys., 11, 507
Kaiser N., Squires G., 1993, ApJ, 404, 441

Kaiser N., Squires G., Broadhurst T., 1995, ApJ, 449, 460
Keeton C. R., Zabludoff A. I., 2004, ApJ, 612, 660
Kelly P. L. et al., 2015, Science, 347, 1123
Koopmans L. V. E., 2004, preprint (arXiv:e-prints)
Lehar J., Hewitt J. N., Burke B. F., Roberts D. H., 1992, ApJ, 384, 453
Lin C.-A., Kilbinger M., Pires S., 2016, A&A, 593, A88
Marshall P., Rajguru N., Slosar A., 2006, Phys. Rev. D, 73, 067302
McCully C., Keeton C. R., Wong K. C., Zabludoff A. I., 2014, MNRAS, 443, 3631
McCully C., Keeton C. R., Wong K. C., Zabludoff A. I., 2017a, ApJ, 836, 141
McCully C., Keeton C. R., Wong K. C., Zabludoff A. I., 2017b, ApJ, 836, 141
Miller C. J. et al., 2001, AJ, 122, 3492
Momcheva I., Williams K., Keeton C., Zabludoff A., 2006, ApJ, 641, 169
Morgan N. D., Kochanek C. S., Pevunova O., Schechter P. L., 2005, AJ, 129, 2531
Nakajima R., Bernstein G. M., Fadely R., Keeton C. R., Schrabback T., 2009, ApJ, 697, 1793
Navarro J. F., Frenk C. S., White S. D. M., 1997, ApJ, 490, 493
Perotto L., Bobin J., Plaszczynski S., Starck J.-L., Lavabre A., 2010, A&A, 519, A4
Petri A., Haiman Z., May M., 2017, Phys. Rev. D, 95, 123503
Pires S., Starck J.-L., Amara A., Teyssier R., Réfrégier A., Fadili J., 2009a, MNRAS, 395, 1265
Pires S., Starck J.-L., Amara A., Réfrégier A., Teyssier R., 2009b, A&A, 505, 969
Pires S., Mathur S., García R. A., Ballot J., Stello D., Sato K., 2015, A&A, 574, A18
Planck Collaboration XIII et al., 2016, A&A, 594, A13
Plaszczynski S., Lavabre A., Perotto L., Starck J.-L., 2012, A&A, 544, A27
Refsdal S., 1964, MNRAS, 128, 307
Reid M. J., Braatz J. A., Condon J. J., Lo K. Y., Kuo C. Y., Impellizzeri C. M. V., Henkel C., 2013, ApJ, 767, 154
Riess A. G. et al., 2016, ApJ, 826, 56
Rodney S. A. et al., 2015, ApJ, 811, 70
Rowe B. T. P. et al., 2015, Astron. Comput., 10, 121
Rusu C. E. et al., 2017, MNRAS, 467, 4220 (H0LiCOW III)
Schild R. E., 1990, AJ, 100, 1771

Schneider P., Sluse D., 2013, A&A, 559, A37
Schneider P., Kochanek C., Wambsganss J., 2006, Gravitational Lensing: Strong, Weak and Micro. Springer-Verlag, Berlin Heidelberg
Sluse D., Hutsemékers D., Courbin F., Meylan G., Wambsganss J., 2012, A&A, 544, A62
Sluse D. et al., 2017, MNRAS, 470, 4838
Springel V., 2005, MNRAS, 364, 1105
Springel V. et al., 2005, Nature, 435, 629
Starck J.-L., Murtagh F., 2006, Astronomical Image and Data Analysis, Cambridge Univ. Press, Cambridge
Starck J.-L., Murtagh F., Pirenne B., Albrecht M., 1996, PASP, 108, 446
Starck J.-L., Murtagh F., Querre P., Bonnarel F., 2001, A&A, 368, 730
Starck J.-L., Pires S., Réfrégier A., 2006, A&A, 451, 1139
Starck J.-L., Fadili M. J., Rassat A., 2013, A&A, 550, A15
Suyu S. H., Marshall P. J., Auger M. W., Hilbert S., Blandford R. D., Koopmans L. V. E., Fassnacht C. D., Treu T., 2010, ApJ, 711, 201
Suyu S. H. et al., 2013, ApJ, 766, 70
Suyu S. H. et al., 2017, MNRAS, 468, 2590
Takada M., Jain B., 2003, MNRAS, 344, 857
Treu T., Marshall P. J., 2016, A&AR, 24, 11
Utsumi Y., Miyazaki S., Geller M. J., Dell'Antonio I. P., Oguri M., Kurtz M. J., Hamana T., Fabricant D. G., 2014, ApJ, 786, 93
Vale C., Hoekstra H., van Waerbeke L., White M., 2004, ApJ, 613, L1
van Waerbeke L., 2000, MNRAS, 313, 524
Vanderriest C., Schneider J., Herpe G., Chevreton M., Moles M., Wlerick G., 1989, A&A, 215, 1
Vikram V. et al., 2015, Phys. Rev. D, 92, 022006
Wilson M. L., Zabludoff A. I., Ammons S. M., Momcheva I. G., Williams K. A., Keeton C. R., 2016, ApJ, 833, 194
Wilson M. L., Zabludoff A. I., Keeton C. R., Wong K. C., Williams K. A., French K. D., Momcheva I. G., 2017, ApJ, 850, 94
Wisotzki L., Christlieb N., Bade N., Beckmann V., Köhler T., Vanelle C., Reimers D., 2000, A&A, 358, 77
Wisotzki L., Schechter P. L., Bradt H. V., Heinmüller J., Reimers D., 2002, A&A, 395, 17
Wong K. C. et al., 2017, MNRAS, 465, 4895

This paper has been typeset from a TEX/LATEX file prepared by the author.